Effective quantum inertia of charge carriers in a macroscopic conductor

A Delgard, B Chenaud, U Gennser, D Mailly, P Degiovanni, C Chaubet

Effective quantum inertia of charge carriers in a macroscopic conductor

A. Delgard[1], B. Chenaud[1], U. Gennser[2], D. Mailly[2], P. Degiovanni[3] and C. Chaubet[1]
[1] *Université Montpellier 2, Laboratoire Charles Coulomb UMR5221, F-34095, Montpellier, France*
CNRS, Laboratoire Charles Coulomb UMR5221, F-34095, Montpellier, France
[2] *Centre de Nanosciences et de Nanotechnologies (C2N), CNRS,*
Université Paris-Sud, Université Paris-Saclay, 91120 Palaiseau, France and
[3] *Univ Lyon, Ens de Lyon, Université Claude Bernard Lyon 1,*
*CNRS, Laboratoire de Physique, F-69342 Lyon, France.**

We study the low frequency admittance of a quantum Hall bar of size much larger than the electronic coherence length. We find that this macroscopic conductor behaves as an ideal quantum conductor with vanishing longitudinal resistance and purely inductive behavior up to $f \lesssim 1\,\mathrm{MHz}$. Using several measurement configurations, we study the dependence of this inductance on the length of the edge channel and on the integer quantum Hall filling fraction. The experimental data are well described by a scattering model for edge magnetoplasmons taking into account effective long range Coulomb interactions within the sample. This demonstrates that the inductance's dependence on the filling fraction arises from the effective quantum inertia of charge carriers induced by Coulomb interactions within an ungated macroscopic quantum Hall bar.

PACS numbers: 72.10.-d, 73.23.-b,73.43.-f, 73.43.Fj

By demonstrating that macroscopic conductors could exhibit robust d.c. transport properties of quantum origin, the integer quantum Hall effect (IQHE) [1–5] has been a major surprise. The importance of this breakthrough for metrology has been acknowledged immediately [1] and has lead to the redefinition of the Ohm at the CPEM88 conference [6]. The finite frequency response of quantum Hall conductors has been a subject of intense work by metrologists: the use of an a.c. bridge at finite frequency f revealed departure of the Hall resistance $R_H(f)$ at $\nu = 2$ from the expected value $R_K/2 = h/2e^2$ [7–11]. It was then attributed to "intrinsic inductances and capacitances" [12, 13]. Later, Schurr *et al* proposed a double shielded sample allowing for a frequency-independent resistance standard [14], but these works left open the question of the origin of these capacitances and inductances.

On the other hand, the finite frequency transport properties of quantum coherent conductors, of size smaller than the electron coherence length, are expected to be dominated by quantum effects. For low-dimensional conductors such as carbon nanotubes [15], or graphene [16], the inductance is of purely kinetic origin. Small superconducting inductors [17, 18] which are now used in space industry [19] are based on the inertia of Cooper pairs. For a quantum coherent conductor, the quantum transport theory developped by Bűttiker and his collaborators [20–22] relates the associated R/L or RC times to the Wigner-Smith time delay for charge carriers scattering across the conductor. These remarkable predictions have been confirmed by the measurement of the finite frequency admittance of quantum Hall R-C [23] and R-L [24, 25] circuits of µm-size in the GHz range at cryogenic temperatures.

In this letter, we demonstrate that, in the a.c. regime, a mm long ungated macroscopic quantum Hall bar, of size much larger than the electronic coherence length, exhibits a finite inductance as well as a vanishing longitudinal resistance. Such a purely inductive longitudinal response is expected for quantum conductors with zero backscattering: a kinetic energy cost proportional to the square of the current arises from both the Pauli principle and the linear dispersion relation for electrons close to the Fermi level. This effective inertia of carriers causes the current response to lag the applied electric field. Here, we identify an inductance of the order of tens of $\mu\mathrm{H\,mm^{-1}}$ and connect it to an effective velocity v_0 of charges along the quantum Hall bar's edges. Contrary to gated samples, in which this velocity is independant of the filling fraction [24], we show that, because of Coulomb interactions between opposite edges of the sample, it does depend on ν in our samples. Using the edge-magnetoplasmon scattering approach combined with a discrete element approach *à la* Bűttiker, we show that, for a sample of width W

$$\frac{v_0}{v_D} = 1 + \frac{\nu\alpha_{\mathrm{mat}}}{\pi}\ln\left[\frac{W/\xi_H}{\nu}\right] \qquad (1)$$

where $v_D = E_y/B_z$ is the drift velocity of non-interacting electrons at the edge, which plays the role of a Fermi velocity in their 1D linear dispersion relation along the edge [26] and α_{mat} denotes the fine structure constant (α_{qed} in the vacuum) within the material: $\alpha_{\mathrm{mat}} = (\alpha_{\mathrm{qed}}/\varepsilon_r) \times (c/v_D)$. The length ξ_H is an effective renormalized width of a single edge channel of the order of the width of incompressible edge channels $\lambda_H = \hbar/m^* v_D$ [27] where $m^* = 0.067\,m_e$ is the effective mass of electrons. Our experimental data leads to estimates for v_D and ξ_H consistent with previous works in similar samples.

Our work demonstrates that the purely inductive response of the macroscopic ungated quantum Hall bar

* Corresponding Author : christophe.chaubet@umontpellier.fr

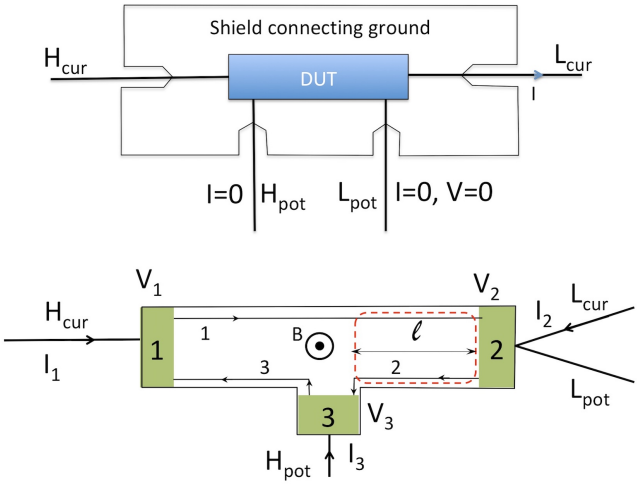

FIG. 1. a) The Device Under Test (DUT) is measured using four coaxial cables and the impedance-meter Agilent HP4294A, which measures the current I at $L_{\rm cur}$, the potential V at $H_{\rm pot}$, and gives $G = I/V$, for details see Ref. [30, 31]. Note that the potentials of $H_{\rm pot}$, $L_{\rm pot}$, $H_{\rm cur}$ and $L_{\rm cur}$ are the potentials of the four connectors of the impedance-meter. b) Scheme of the multi-terminal Hall bar with only three ohmic contacts wire-bonded onto the sample holder. In this geometry, the impedance is $Z_{23}^{(\rm exp)}(\omega) = -(\partial V_3/\partial I_2)(\omega)$ for $V_2 = 0$.

reflects the effective quantum inertia of charge carriers renormalized by Coulomb interactions within the sample. Therefore, although electron transport across such a conductor is not coherent, its d.c. and a.c. transport properties are of quantum origin, a fact that ultimately relies on the coherence of edge magnetoplasmon (EMP) modes propagating along chiral edge channels. EMP coherence has enabled the demonstration of single and double EMP Fabry-Pérot interferometers [28] as well as of a Mach-Zehnder plasmonic interferometer [29].

Our samples are processed on an AlGaAs/GaAs heterojunction with the two dimensional electron gas (2DEG) located at the hetero-interface with carrier density $N_s = 5.1 \times 10^{11}\,\mathrm{cm}^{-2}$ and mobility $\mu = 30\,\mathrm{m}^2/\mathrm{Vs}$. We have processed a 400 µm wide ungated Hall bar whose large size was necessary in order to exhibit a sufficiently large kinetic inductance. The sample is placed at the center of a high magnetic field at the temperature of pumped He_4 (1.5 K).

A measurement setup of impedance is depicted on Fig. 1-a.: the current is injected using $H_{\rm cur}$, and measured using $L_{\rm cur}$. The potential of $H_{\rm pot}$ is measured while $V = 0$ and $I = 0$ are imposed at $L_{\rm pot}$. All measurements were performed using an impedance-meter Agilent 4294A [30, 31] in the nominal conditions for accurate measurements. The amplitude of the voltage applied across the sample was 5 mV. In the IQHE regime, this induces a current intensity below 0.5 µA at $\nu = 2$, a value far below the breakdown current and even far below current densities used in metrology [4, 7]. For each values of magnetic field, the resistance and the reactance have been measured for 300 values of the frequency f in the range 40 Hz-100 kHz.

Due to chirality of the quantum Hall transport, an ohmic contact wire-bonded to the sample holder and so to a coaxial cable, generates a leakage current through the cable capacitance if the potential does not vanish [32, 33]. This results in a faulty measurement [34, 35]. For this reason, all results presented here have been carried out at integer filling factors, where the longitudinal resistance $R_{xx}(\omega)$ vanishes[36]. Furthermore, only a few of the ohmic contacts processed on the sample were wire-bonded onto the sample holder as shown on Fig. 1.b. In order to measure the zero resistance state, a third contact is inserted along the edge connected to the reference potential (contact 2 on Fig. 1.b). In d.c., one would measure a potential $V_{\rm H_{pot}} = 0$. In a.c., $V_{\rm H_{pot}} \neq 0$ and we measure the frequency dependent impedance $Z_{23}^{(\rm exp)}(\omega) = -\partial V_3/\partial I_2|_{V_2=0}(\omega)$. Different configurations can be obtained, by changing the location of the third contact and the sample side. In this case, the magnetic field orientation also has to be changed. In order to access the dependence on the lengths of the edge channels, we have investigated several configurations, which entailed shifting the ohmic contacts on the holder. Sometimes, we have also wire-bonded a fourth ohmic contact on the same side of the sample to connect $L_{\rm pot}$ to access another edge channel length.

Figure 2 presents unfiltered and non-averaged raw data for the frequency dependent reactance $X(f) = \mathrm{Im}(Z_{23}^{(\rm exp)}(2\pi f))$ in a given sample configuration for integer filling factors $\nu = 2, 4, 6, 8$. The positive linear dependence of $X(f)$ is the signature of an inductive behavior. The corresponding inductance decreases with filling factor. These data are completely reproducible in the regions of magnetic fields as long as $R_{xx} = 0$. This is a key point of our work: for all filling factors, the real part $R(f) = \mathrm{Re}(Z_{23}^{(\rm exp)}(2\pi f))$ of the measured impedance is close to zero with values between $\pm 0.5\,\Omega$ at low frequency as shown in the inset of Fig. 2. These results extend the work of Gabelli *et al* [24] in which the sample resistance was $R_H = R_K/\nu$, to the case of a zero resistance macroscopic device. At higher frequencies, a small real part of the measured response function $R(f)$ appears. This effect is discussed in the Supplementary Material (Sec. 2) and is correlated to the deviation of the reactance $X(f)$ from linearity seen on Fig. 2.

Let us now explain how this inductive behavior arises from the quantum inertia of carriers renormalized by Coulomb interactions within the quantum Hall bar. In the presence of an a.c. drive, the propagation of electric charges is described by the dynamics of charge density waves (plasmons) whose velocity in 1D or 2D systems is modified by Coulomb interactions. The idea is that the ac drive applied to the reservoir injects a classical plasmon wave into the conductor. Knowing how this incoming wave is scattered by the conductor enables us to compute the corresponding outgoing currents and consequently, the electrical current flowing across all leads and gates connected to the conductor. This general idea

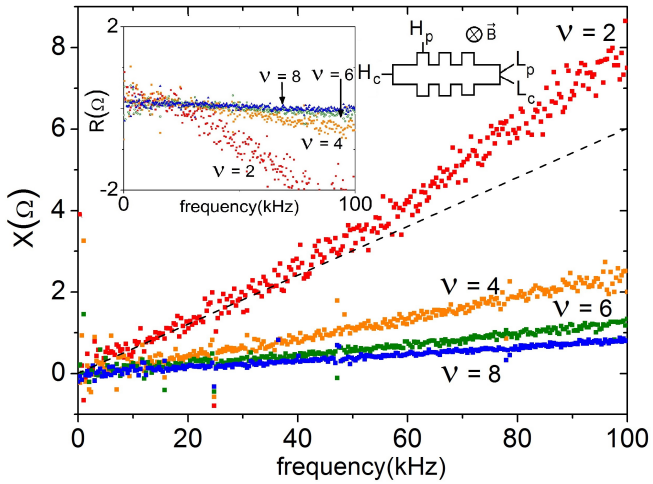

FIG. 2. The reactance $X(f)$ as a function of the frequency f for different filling factors and $B_{<0}$, in the measurement configuration shown here. Inset: the longitudinal resistance $R(f)$ vanishes quadratically for integer filling factors at low frequency.

was first applied to 1D gated quantum wires by I. Safi who has related its finite frequency admittance matrix to the scattering matrix of plamons propagating within the wire [37, 38]. It has lead to remarkable predictions on fractionalization of charge pulses [39] observed only a decade ago [40]. Fractionalization has also been studied in an artificial Tomonaga-Luttinger liquid obtained from two capacitively coupled counter-propagating edge channels in AlGaAs/GaAs heterostructures [41] as well as in graphene [42]. More recently, time of flight measurements have probed the dynamics of plasmon modes in quasi-1D wires made from a tailored 2DEG at zero magnetic field and confirmed the role of Coulomb interactions in this system [43].

In the context of the quantum Hall effect, the relevant degrees of freedom are EMP modes which have been studied since the 80s [44–46]. The edge-magnetoplasmon scattering approach has been used to describe the high frequency linear response of circuits built from quantum Hall edge channels [47]. It has also been used for discussing energy relaxation in a $\nu = 2$ edge channel system [48, 49] and it is the key ingredient for predicting single electron decoherence in quantum Hall edge systems [50].

We have developped an analytical model for edge-magnetoplasmon scattering in the spirit of Ref. [28] for a quantum Hall bar taking into acccount long range Coulomb interactions between edge channels of the same chirality as well as between counter-propagating edge channels. This effective edge-magnetoplasmon scattering model, analytically solved in the Supplementary Material (Sec. 3), describes the finite frequency transport in the linear regime beyond the GHz, the limit being the cyclotron frequency which is 4 THz at 1 T. Above it, inter-Landau level transitions may be excited and the bulk contribution cannot be neglected. To account for the long-range interactions in our ungated quantum Hall bars, this model assumes that all the edge channels of the same chirality have the same velocity v_D and are so strongly coupled that they see the same time independant potentiel as in Ref. [25]. The two counterpropagating groups of edge channels are capacitively coupled by a geometric capacitance C_H. Finally, dissipation of EMP modes have been neglected, an hypothesis a posteriori satisfied in our samples.

In the geometry of the sample depicted on Fig. 1, the low frequency expansion of the measured reactance is of the form (see Supplementary Material, Sec. 2):

$$\mathrm{Im}\left(Z_{23}^{(\mathrm{exp})}(\omega)\right) = \mathrm{i}L\omega + \mathcal{O}(\omega^2) \tag{2}$$

where L denotes the total inductance for the quantum Hall bar delimited by a dashed red box on Fig. 1-b. Because the magnetic inductance L_m is much smaller than the kinetic inductance L_kin in our sample (see Supplementary Material, Sec. 1), $L = L_\mathrm{m} + L_\mathrm{kin} \simeq L_\mathrm{kin}$ can be obtained from the edge magnetoplasmon scattering model as

$$L = (R_K/\nu) \times (l/2\,v_0) \tag{3a}$$

$$v_0 = v_D \times \left(1 + \frac{C_q}{2C_H}\right). \tag{3b}$$

where l is the length of the Hall bar (see Fig. 1-b), $C_q = \nu e^2 l/h v_D$ is the quantum capacitance of ν edge channels and the geometric capacitance C_H describes the effect of Coulomb interactions between counter propagating edge channels. This is different from the quantum RL-circuit where, because of the gating, the capacitance C_H has to be replaced by the capacitance with the nearby gates leading to a renormalization of v_D by $1 + C_q/C_H$ for right and left moving charge density waves [24]. Here, by contrast, the renormalization corresponds to the ratio of a C_H capacitance with the series addition $C_q/2$ of the quantum capacitances of counterpropagating edges. Eq. (3) suggests that the inductance can be interpreted as a kinetic inductance associated with an effective time of flight l/v_0. As discussed in the Supplementary Material (Sec. 3), v_0 is neither the drift velocity for non-interacting electrons nor even a renormalized electron's velocity within chiral edge channels but an effective velocity arising from the combination of their quantum inertia and Coulomb interactions within the quantum Hall bar. This inertia is of quantum origin, reflecting the minimal energy associated with an electrical current due to Fermi statistics of electrons, augmented here by the effects of Coulomb interactions.

At fixed v_D, the main ν-dependence of v_0 arises from the linear increase of C_q with ν in (3b) but we expect a sublinear ν-dependence coming from the dependence of the geometric capacitance C_H on the structure and geometry of the quantum Hall edge channels. In the Supplementary Material (Sec. 4), we show that the main subdominant contribution induced by the geometric capacitance dependence on ν, which arises from the linear

dependence on ν of the width of the edge channels, is logarithmic:

$$C_H(\nu, l) = \frac{\pi \varepsilon_r \varepsilon_0 l}{\ln\left[\frac{W/\xi_H}{\nu}\right]} \tag{4}$$

where W denotes the sample width and ξ_H is a length proportional to the width W_H of a single quantum Hall edge channel. Following Ref. [27], $W_H = (1 + \pi^2 \alpha_{\rm mat})\hbar/m_* v_D$, which is of the order of a few tens of nm for AlGaAs/GaAs quantum Hall systems. The dimensionless factor ξ_H/W_H depends on the specific microscopic model used to describe the edge channel geometry [27, 51]. Eq. (4) can therefore be considered as a universal scaling formula leading to the ν-dependence of v_0 for ungated samples given by Eq. (1).

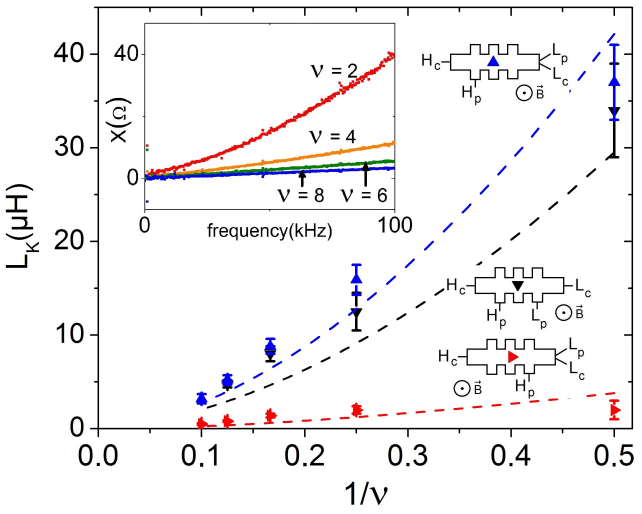

FIG. 3. (Color online) For three measurement configurations with $B > 0$ depicted on the figure, the inductance increases with $1/\nu$ as expected by Eq. (3a). Dashed lines correspond to our theory for (red data) $l = 600\,\mu$m with $v_D = 8 \times 10^5\,\mathrm{ms}^{-1}$, (black data) $l = 1000\,\mu$m with $v_D = 0.16 \times 10^5\,\mathrm{ms}^{-1}$ and (blue data) $l = 1600\,\mu$m with $v_D = 0.2 \times 10^5\,\mathrm{ms}^{-1}$. Inset: reactance $X(f)$ as a function of the frequency for different filling factors and $B > 0$.

Let us now compare this prediction to the experimental data. Fig. 3 contains the first main quantitative result of this work, *i.e.* the quantum inductance as function of $1/\nu$ for configurations $B > 0$. Values have been obtained from the reactance data depicted on Fig. 2 and on the inset of Fig. 3 using the slope at low frequency of $f \mapsto X(f)$ datasets. Three configurations in which $L_{\rm pot}$ and $H_{\rm pot}$ are plugged to different contacts (see Fig. 3) have been studied. The main result is the dependence of the inductance on $1/\nu$ which is increasing but with a slight non-linearity according to Eq. (3b) and (4).

To verify this sub-dominant behavior, we have extracted the velocity v_0 using Eq. (3a) from each value of the inductance. These values are reported in Fig. 4 as a function of ν. This is the second main quantitative experimental result of this work. Each family of points corresponds to a specific sample configuration for which the sample has been heated up, re-bonded and cooled down again. These manipulations affect the electrostatic arrangement of charges at the edge, thereby modifying v_D from one experiment to the other. Fig. 4 thus presents predictions for $v_0(\nu)$ from Eq. (1) for different values of v_D. Using five different values of v_D as a single fit parameter in Eq. (1) for five different sets of experimental data gives the dashed lines on Fig. 4. This demonstrates a good agreement between the experimental results for v_0 as a function of ν deduced from admittance measurements using Eqs. (3) and predictions from Eq. (1). The highest values of v_D obtained here are comparable to the ones obtained on ungated samples (as ours) in Ref. [52] but five times higher than those in Refs. [24, 53] obtained on samples with side gates. This is expected since gating leads to a higher geometric capacitance which brings down the velocity v_0 much closer to v_D. Last but not least, because of the variabilty of the electrostatic environment in ungated samples, the spread of values for v_D found here is not surprising because the datasets depicted on Fig. 4 correspond to different experiments performed on both sides of the sample. Additional results obtained on samples from different wafers are presented in Sec. 5 of the Supplementary Information provide additional evidence of the robustness of our analysis.

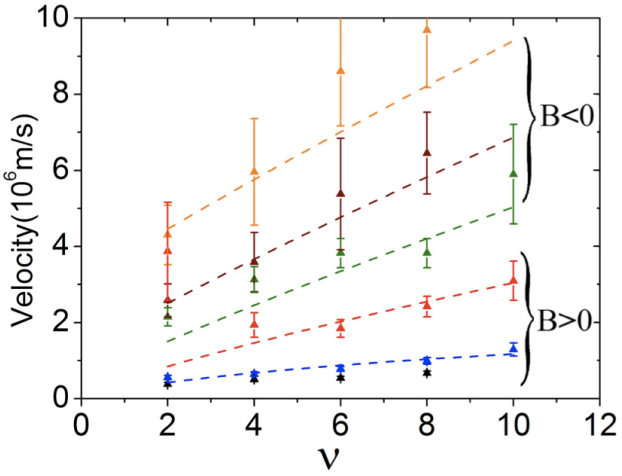

FIG. 4. Low frequency charge carrying edge-magnetoplasmon velocity v_0 as a function of filling factor ν. Dashed curves correspond to Eq. (1) for the values, from bottom to top, $v_D = (0.15; 0.8; 4; 12; 30) \times 10^5\,\mathrm{ms}^{-1}$.

To summarize, we have shown that, at low frequencies, a macroscopic quantum Hall bar is a perfect 1D conductor exhibiting a vanishing longitudinal resistance and a finite inductance. By fitting its dependence on the filling fraction and on the sample geometry using a simple long range effective Coulomb interaction model, we have shown that it reflects the effective quantum inertia of charge carriers within the edges of the quantum Hall bar. Contrary to the case of superconductors where carrier in-

ertia arises from the effective mass of the Cooper pairs, here it reflects how Coulomb interactions alter the propagation of low-frequency massless edge-magnetoplasmon modes. A quantum Hall bar of size much larger than the electron's coherence length thus appears as a quantum conductor not only in the d.c. regime but also at low frequencies in the a.c. regime. Although the low frequency response is not universal, its dependence on the filling fraction and sample geometry can be understood using a simple model which is formally similar to the one used for gated nano-fabricated samples [47]. Therefore macroscopic samples can provide a rescaled test-bed for studying the scattering properties of edge-magnetoplasmons in µm-sized quantum coherent samples. Studying a.c. transport properties of macroscopic samples up to radio-frequencies could thus open the way to realizing controlled quantum linear components for quantum nanoelectronics in 1D edge channels, with possible applications to electron [54] and micro-wave quantum optics in ballistic quantum conductors [55].

ACKNOWLEDGMENTS

We warmly thank G. Fève, Ch. Flindt and B. Plaçais for useful discussions and suggestions concerning this manuscript. This work has been partly supported by ANR grant "1shot reloaded" (ANR-14-CE32-0017).

Supplementary Information

In this Supplementary Information, we discuss a simple evaluation of the kinetic inductance of a quantum Hall bar at filling fraction ν, compare it to its geometric inductance. We then move directly towards a more realistic evaluation of experimental relevant quantities. First, we connect these quantities to the way a quantum Hall bar scatters ac currents. To compute this scattering properties, we use the edge magnetoplasmon scattering method which takes into account Coulomb interactions between the opposite channels of the quantum Hall bar. Moreover, we connect these scattering properties to the finite frequency admittance of the quantum Hall bar.

Appendix A: Kinetic and magnetic inductance

In this section, we compare the kinetic inductance of a quantum Hall bar at filling fraction ν to its geometric inductance.

1. Kinetic inductance

Let us first consider non-interacting chiral charge carriers with propagation velocity v_D (see Fig. 5). A net current flow corresponds to a chemical potential between chiral edge channels of opposite chirality. The corresponding kinetic energy is then obtained by adding together the energy of all quantum states which have been occupied when biasing chiral edge states with different chemical potential $\Delta\mu = -eV$:

$$E_{\rm chir} = \sum_k \varepsilon(k) = \nu \times g(\varepsilon) l \times (eV)^2/2\,, \qquad \text{(A1)}$$

where $g(\varepsilon) = 1/hv_D$ is the density of states (DOS) per unit length for a 1D-channel, ν the number of channels, l the edge-state length. The voltage drop across the sample is $V = R_H I_\nu$, where $R_H = R_K/\nu = h/e^2\nu$ denotes the quantum Hall resistance at filling fraction ν and I_ν the current. The resulting kinetic energy is then quadratic in the current, as expected for a linear inductor:

$$E_{\rm chir}(I_\nu) = \frac{\nu e^2}{hv_D} \times \frac{l}{2} \times \left(\frac{R_K I_\nu}{\nu}\right)^2 = \frac{h}{e^2} \times \frac{l}{\nu v_D} \times \frac{I_\nu^2}{2}\,. \qquad \text{(A2)}$$

For a quantum Hall bar, we have two counter-propagating groups of ν chiral edge channels. Assuming that the two chiralities carry equal charge of the total current $I_\nu = \pm I/2$, this leads to a total kinetic energy

$$E_K(I) = 2E_{\rm chir}(I/2) = \frac{h}{e^2} \times \frac{l}{\nu v_D} \times \frac{2(I/2)^2}{2}\,. \qquad \text{(A3)}$$

Using $E_K(I) = LI^2/2$, we obtain the following formula for the inductance L of the quantum Hall bar:

$$L_K = \frac{R_K}{\nu} \times \frac{l}{2v_D} \qquad \text{(A4)}$$

Note the appearance of the half of the time of flight l/v_D of the electrons across the quantum Hall bar which is ultimately due to the existence of two counter-propagating groups of copropagating edge channels.

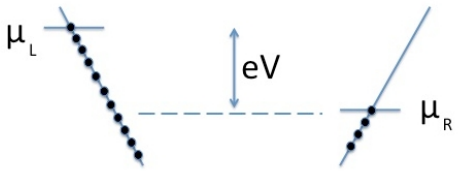

FIG. 5. Dispersion relations for non-interacting electrons propagating along a right-moving chiral edge channel R and a left moving one L with propagation velocity $\pm v_D$. In the presence of a d.c. voltage bias V, a chemical potential imbalance $-eV$ appears between the two chiral edge channels. At filling fraction ν, such a bias generates a net current $I = (e^2\nu/h)\times V$.

2. Magnetic inductance

A quantum Hall bar can be viewed as a conductor built from two linear wires of length l, and of diameter or width

W_H separated by a distance W which is the width of the quantum Hall bar. The magnetic inductance of the resulting dipole can be computed from Biot-Savart's law [56]. Note that the wire's diameter $W_H(\nu)$ usually scales as ν (see Ref. [27] and Sec. D 1). In the quantum Hall bar geometry, the total current I flowing across the quantum Hall bar corresponds to $\pm I/2$ along each of the two long counter-propagating edges. Consequently, in the limit $l, W \gg W_H(\nu)$, the geometric inductance of the quantum Hall bar is approximately equal to

$$L_{\rm m} = \frac{l\mu}{\pi}\left[\ln\left(\frac{2W}{W_H(\nu)}\right) - 1\right] \tag{A5}$$

where $\mu = \mu_r\mu_0$ is the magnetic permeability of the material expressed as the product of its relative permeability μ_r by the vacuum permittivity $\mu_0 = 1/\varepsilon_0 c^2$. For a non-magnetic material such as AlGaAs/GaAs, $\mu_r = 1$ and therefore $\mu = \mu_0$.

Using this expression and Eq. (A4), the ratio of the magnetic to the kinetic inductance is given by:

$$\frac{L_{\rm m}}{L_K} = 4\alpha_{\rm qed}\,\frac{v_D}{c} \times \nu \times \left[\ln\left(\frac{2W}{W_H(\nu)}\right) - 1\right] \tag{A6}$$

where $\alpha_{\rm qed}$ is the fine structure constant. The magnetic character of this ratio appears through the multiplication factor $v_D/c \ll 1$. Together with the smallness of $\alpha_{\rm qed}$ and the logarithmic dependance in the aspect ratio $W/W_H(\nu) \sim W/\nu W_H(1)$, this explains why the magnetic inductance is always much smaller than the kinetic one for $\nu \lesssim 100$.

Appendix B: Experimental signals

In this section, we discuss how the quantities that are measured in the experiment are related to the a.c. response of a quantum Hall bar even in the presence of experimental imperfections such as cable capacitances.

1. Finite frequency transport in quantum Hall edge channels

In his pioneering work on finite frequency charge transport in mesoscopic conductors [20], Büttiker stressed the importance of interactions: time dependent drives applied to reservoirs lead to charge pumping in the conductor which, in return, alter the electrical potential within the conductor. As a result, its transport properties can no longer be derived by using the d.c. response at zero bias. Büttiker then developed a self consistent mean-field approach to this problem, taking into account how the time dependent charge density within the conductor generates a time-dependent potential and thereby alters the transport [22]. In the linear regime, the a.c. response of the conductor is described by the admittance matrix

$$G_{\alpha\beta}(\omega) = \left.\frac{\partial I_\alpha(\omega)}{\partial V_\beta}\right|_{V=0} \tag{B1}$$

giving the average current entering the conductor from lead α when a voltage drive at the same frequency $\omega/2\pi$ is applied to the reservoir β. Charge conservation and gauge invariance imply that the finite frequency admittance matrix satisfy the general sum rules

$$\sum_\alpha G_{\alpha\beta}(\omega) = 0 \tag{B2a}$$

$$\sum_\beta G_{\alpha\beta}(\omega) = 0 \tag{B2b}$$

which is ensured by total screening of effective Coulomb interactions.

At low frequency, this admittance matrix is expanded in ω, the zero-th order term being its d.c. conductance $G^{\rm (dc)}_{\alpha\beta}$. The first order term is related to the emittances introduced by Büttiker *et al.* :

$$G_{\alpha\beta}(\omega) = G^{\rm (dc)}_{\alpha\beta} - {\rm i}\omega E_{\alpha\beta} + \mathcal{O}(\omega^2)\,. \tag{B3}$$

For quantum Hall edge channels, Christen and Bűttiker [57] fully exploited the chirality of charge transport to compute the dc conductances $G^{\rm (dc)}_{\alpha\beta}$ as well as the emittances $E_{\alpha\beta}$ using a discrete element description of the circuit.

Here we will show how to describe the finite frequency transport using the building blocks of a discrete element description of quantum Hall bars and the finite frequency admittance properties obtained from the edge-magnetoplasmon (EMP) scattering approach. The latter has been first pioneered in the context of quantum wires [37, 38] before being used for quantum Hall edge channels [48] where it is instrumental for computing single electron decoherence [50, 58]. The details of how the admittances are obtained from the EMP scattering approach will be described later in Sec. C.

Depending on the sign of the diagonal emittances, the quantum conductor under consideration exhibits a capacitive ($E_{\alpha\alpha} > 0$) or inductive ($E_{\alpha\alpha} < 0$) behavior. Basic examples of these behaviors, involving two different two-contact devices, have been given by Christen and Bűttiker [57]. A two-contact Hall bar is predicted to act as an inductance while a ring shaped sample (the so-called Corbino geometry) acts as a capacitance. Hence both geometries exhibit opposite diagonal emittances, which can be understood in terms of reaction of the circuit to an injected charge. Indeed, as shown on Fig. 1 of [57] a charge injected by contact 1 into a Hall bar is transmitted to contact 2, while the charge induced by inter-edge Coulomb interactions created at contact 2 is transmitted to contact 1. On the contrary, in a Corbino sample, the injected charge returns to the contact it comes from, as does the image charge. It was experimentally shown by Delgard *et al.* [59] that Corbino emittances will exhibit this predicted capacitive behavior. Here, we will highlight the inductive behavior of quantum Hall bars in a multi-contact geometry that ensures vanishing longitudinal resistance.

We shall now discuss how, for two different sample configurations, the measured response function relates to the finite frequency admittance of the quantum Hall bar depicted as a red dashed rectangle in the two forthcoming figures, taking into account capacitive leaks at the contacts.

2. Three contact geometry

Let us first consider the three contact geometry depicted on Fig. 6. Contacts 1 and 2 are directly connected to reservoirs whereas contact 3 is not but we take into account the cable capacitance C_0 of the cable. In this section, we shall compute the experimentally measured finite frequency impedance

$$Z_{23}^{(\mathrm{exp})}(\omega) = -\left.\frac{\partial V_3(\omega)}{\partial I_2(\omega)}\right|_{V_2=0} \tag{B4}$$

up to second order in ω and show how it relates to the properties of the quantum Hall bar B and to the cable capacitance C_0 (see Fig. 6).

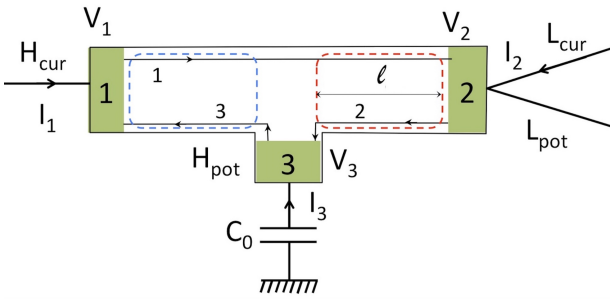

FIG. 6. The device under test when three Ohmic contacts are wire-bonded onto the sample holder. The quantum Hall bar B, which is the dipole under test, is shown as a dashed red box. The quantum Hall bar A is shown as a dotted blue box. The capacitance of the coaxial cable connected to contact 3 is denoted by C_0. In this experimental setup, $V_2 = 0$ whereas the drive V_1 is non zero and the experimentally measured impedance is $Z_{23}^{(\mathrm{exp})} = -\partial V_3/\partial I_2$.

a. *Obtaining* $Z_{23}^{(exp)}$

In this approach, the quantum Hall bars A and B delimited on Fig. 6 are characterized by their frequency-dependent EMP scattering matrix. For the quantum Hall bar A, the EMP scattering matrix, which we denote here by $\mathbf{A}(\omega)$ relates the ingoing and outgoing currents through [60]

$$\mathbf{j}^{(\mathrm{out})}(\omega) = \mathbf{A}(\omega)\,\mathbf{j}^{(\mathrm{in})}(\omega) \tag{B5}$$

in which the edges of the Hall bar are labeled by their chirality. In the same way, the EMP scattering matrix of the quantum Hall bar B will be denoted by $\mathbf{B}(\omega)$. These matrices are computed in Sec. C but for the moment, we won't need their explicit form.

At contact 3, the incoming and outgoing currents propagating within the edge channels are also related by an input/output relation that reflects the time delay associated with the $R_H C_0$ relaxation time of the contact:

$$i_{3,\mathrm{out}}(\omega) = \frac{i_{3,\mathrm{in}}(\omega)}{1 - \mathrm{i}R_H C_0 \omega} \tag{B6}$$

Eliminating the edge channel currents internal to the sample directly leads to the finite frequency admittances connecting the currents I_α entering from the reservoirs to the drive voltage V_1:

$$R_H\, I_2 = -\frac{A_{RR}B_{RR}}{1 - A_{RL}\mathcal{T}B_{LR}}\, V_1 \tag{B7}$$

in which the matrix elements of the Hall bar's current scattering matrices $\mathbf{A}$ and $\mathbf{B}$ are involved as well as $\mathcal{T}(\omega) = 1/(1 - \mathrm{i}R_H C_0\omega)$, the edge current transmission of the Ohmic contact with cable capacitance C_0. For simplicity, the ω dependence of V_1, I_2 and of the scattering matrix elements of the A and B quantum Hall bars as well as of $\mathcal{T}$ have been omitted. The potential of the contact 3 can also be computed as

$$-\,\mathrm{i}\omega C_0 R_H\, V_3 = \frac{(\mathcal{T}-1)B_{LR}A_{RR}}{1 - A_{RL}\mathcal{T}B_{LR}}\, V_1 \tag{B8}$$

which finally leads to

$$\frac{Z_{23}^{(\mathrm{exp})}(\omega)}{R_H} = \frac{1}{1 - \mathrm{i}R_H C_0\omega}\,\frac{B_{LR}(\omega)}{B_{RR}(\omega)}\,. \tag{B9}$$

Note that, at low frequency ($\omega R_H C_O \ll 1$), the result only depends on the finite frequency properties of the B quantum Hall bar *i.e.* the dipole under test in this setting.

b. *Effect of the finite frequency deviation of* $Re(Z_{xy}(\omega))$ *from* R_H *on* $Z_{23}^{(exp)}$

It is then useful to relate $Z_{2,3}^{(exp)}$ to the impedance of the Hall bar B, which we know has a real part $\sim R_H$, with a small deviation for $\omega \neq 0$, as observed by metrologists studying the quantum Hall resistance a low frequencies [15-17].

This is achieved using the relation [38, 48] between the quantum Hall bar finite admittance matrix and its edge-magnetoplasmon scattering matrix to obtain the following expression, valid when the left and right moving edges of the quantum Hall bar are in total mutual influence:

$$\frac{Z_{23}^{(\mathrm{exp})}(\omega)}{R_H} = \frac{z_H(\omega) - 1}{1 - \mathrm{i}R_H C_0\omega} \tag{B10}$$

in which $z_H(\omega)$ denotes the dimensionless impedance of the quantum Hall bar B in units of R_H. Note that within

the framework of the edge-magnetoplasmon scattering model presented in Sec. C, $z_H(\omega) = 2Z(\omega)/R_H$ where $Z(\omega)$ is given in terms of the edge-magnetoplasmon scattering matrix by Eq. (C15b). It thus predicts predicts $\mathrm{Re}(z_H(\omega)) = 1$ and therefoe $\mathrm{Re}\left(Z_{23}^{(\mathrm{exp})}(\omega)\right) = 0$.

However, we will now show that a non vanishing $r(\omega) = \mathrm{Re}(z_H(\omega)) - 1$ is responsible for the non-linearity of $X(f)$ seen on Fig. 2 of the paper. Such a feature has been observed for long time by metrologists studying quantum Hall resistance at low frequencies [7, 10, 11]. In the metrology community, this finite frequency deviation $r(\omega)$ from the dc quantum Hall value is commonly attributed to parasitic effects such as self and resistance of ohmic contacts and bond wires and thus depend on configurations and samples. A quadratic dependence on the frequency is usually found in the form $r(\omega) = a_2(\omega/2\pi)^2$. The a_2 parameter has been measured in many configurations and samples and has been found to be positive or negative but is always around (or below) $10^{-7}\,/\mathrm{kHz}^2$ [7, 10, 11].

To discuss the experimental results, which include both the real and imaginary parts of $Z_{23}^{(\mathrm{exp})}(\omega)$, let us therefore write

$$z_H(\omega) = 1 + r(\omega) + \mathrm{i}\omega\tau_H(\omega) \tag{B11}$$

in which $r(\omega)$ denotes the frequency-dependent deviation to R_H (when non zero), and $\tau_H(\omega) = L_{\mathrm{eff}}(\omega)/R_H$ is the dimensionless frequency-dependent effective RL-time of the quantum Hall bar ($L = L_{\mathrm{eff}}(\omega = 0)$). The low frequency expansion of the experimentally measured impedance $Z_{23}^{(\mathrm{exp})}(\omega)/R_H$ is then

$$\frac{Z_{23}^{(\mathrm{exp})}(\omega)}{R_H} \simeq r(\omega) - \omega^2 L_{\mathrm{eff}}(\omega) C_0 \tag{B12a}$$

$$+ \mathrm{i}\omega\left[\frac{L_{\mathrm{eff}}(\omega)}{R_H} + R_H C_0 r(\omega)\right] + \mathcal{O}(\omega^3) \tag{B12b}$$

In our experiments, the reactance $\mathrm{Im}\left(Z_{23}^{(\mathrm{exp})}(\omega)\right)$ is obviously dominated by the kinetic inductance L:

$$\mathrm{Im}\left(Z_{23}^{(\mathrm{exp})}(\omega)\right) = \omega L\,, \tag{B13}$$

but $r(\omega)$ is seen through the deviations of the imaginary part from linearity (see Fig. 2 of the paper). It is nevertheless small and therefore, the dominant contribution to the real part $\mathrm{Re}\left(Z_{23}^{(\mathrm{exp})}(\omega)\right)$ is a negative quadratic one directly proportional to the cable capacitance: $-\omega^2 L C_0$, as observed in the inset of Fig. 2 of the paper.

Both real and imaginary part of admittance seen in Fig. 2 suggest a quadratic behavior for $r(\omega)$. To second order in $\omega R_K C_0$:

$$\mathrm{Re}\left(\frac{Z_{23}^{(\mathrm{exp})}(\omega)}{R_H}\right) = (R_H C_0\omega)^2\left[r_2 - \frac{L/R_H}{R_H C_0}\right] \tag{B14}$$

where $r(\omega) \simeq r_2\,(\omega R_H C_0)^2$.

In our experiments, the cable capacitance is $C_0 = 218\,\mathrm{pF}$. We deduce from Fig. 2 of the paper that, at $\nu = 2$ and $\omega/2\pi = 100\,\mathrm{kHz}$, $\omega r(\omega) R_H^2 C_0 \approx 2.2\,\Omega$. This gives $r(\omega) \approx 10^{-4}$ at $100\,\mathrm{kHz}$ thereby corresponding to $a_2 = 4\pi^2 r_2 (R_H C_0)^2 \approx 10^{-8}\,/\mathrm{kHz}^2$, a value in total agreement with the deviations reported in the litterature. Consequently, the observed deviations from pure inductive behavior can be explained by the combined effect of the cable capacitance and of the deviations of $\mathrm{Re}(Z_H(\omega))$ from its dc value R_H.

3. Four contact geometry (two on the same side)

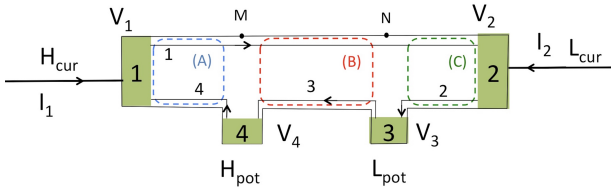

FIG. 7. The device under test has now four contacts connected to sample holder, two of them being on same side. The quantum Hall bar is divided into three parts, shown as colored box, A (blue), B(red) and C(green). H_{pot} and L_{pot} are connected respectively to contacts 4 and 3. In this configuration, the low frequency impedance depends only on the central Hall bar B.

Let us now turn to the case of a four contact sample depicted on Fig. 7. This geometry represent a four contact measurement of the central part B of the device. Here, the parts A and C of the device play the role of the leads that connect B to the current injection reservoirs which are the Ohmic contacts 1 and 2. The Ohmic contacts 3 and 4 are used for measuring the voltage difference between the two port of the would-be dipole B.

In this section, the capacitances C_0 of the cables will be omitted for simplicity. This does not change the physics of the problem but greatly simplifies the computations. Nonetheless, we know from Eq. (B6) that the same prefactor $(1 - \mathrm{i}R_H C_0\omega)^{-1}$ will appear in the results when capacitances are taken into account.

We assume that A, B and C can be modeled as quantum Hall bars characterized by their edge-magnetoplasmon scattering matrices. Exactly as before, this amounts to neglecting Coulomb interactions outside the Hall bars themselves, an hypothesis consistent with the total screening hypothesis stated in Sec. C 1. Let us denote by M and N the points on edge channel 1, which respectively face contacts 4 and 3. Introducing the EMP scattering matrices $\mathbf{A}$, $\mathbf{B}$ and $\mathbf{C}$ respectively associated with the three quantum Hall bars A, B and C represented on Fig. 7, the dynamics of the three quantum

Hall bars is described by:

$$\begin{pmatrix} i_M \\ i_{4,\mathrm{out}} \end{pmatrix} = A \begin{pmatrix} i_{1,\mathrm{in}} \\ i_{4,in} \end{pmatrix} \tag{B15a}$$

$$\begin{pmatrix} i_N \\ i_{3,\mathrm{out}} \end{pmatrix} = B \begin{pmatrix} i_M \\ i_{3,\mathrm{in}} \end{pmatrix} \tag{B15b}$$

$$\begin{pmatrix} i_{1,\mathrm{out}} \\ i_{2,\mathrm{out}} \end{pmatrix} = C \begin{pmatrix} i_N \\ i_{2,in} \end{pmatrix} \tag{B15c}$$

in which, for compactness, the ω dependence is not recalled. In the experimental configuration depicted in Fig. 7, $V_3 = 0$ and we measure V_4. We calculate I_2 and V_4, in order to find $Z_{42}^{(\mathrm{exp})} = V_4/I_2$. The lead potentials fix the incoming currents injected by the reservoirs. Moreover, because of the high impedance of the voltmeter connected to H_{pot} and L_{pot}, we neglect the currents leaking into these Ohmic contacts. We thus have:

$$i_{1,\mathrm{in}} = G_H V_1, \quad i_{2,\mathrm{in}} = G_H V_2 \tag{B16a}$$

$$i_{3,\mathrm{in}} = 0, \quad i_{4,\mathrm{in}} = G_H V_4 \tag{B16b}$$

$$i_{3,\mathrm{in}} = i_{2,\mathrm{out}}, \quad i_{4,\mathrm{in}} = i_{3,\mathrm{out}} \tag{B16c}$$

$$I_2 = i_{2,\mathrm{in}} - i_{1,\mathrm{out}}. \tag{B16d}$$

From Eqs. (B15a) and (B15b), we obtain :

$$\begin{aligned} G_H V_4 &= i_{4,\mathrm{in}} = i_{3,\mathrm{out}} \\ i_{3,\mathrm{out}} &= B_{LR}(A_{RR} G_H V_1 + A_{RL} G_H V_4) \end{aligned} \tag{B17}$$

or, equivalently:

$$V_4 = \frac{B_{LR} A_{RR}}{1 - B_{LR} A_{RL}} V_1 \,. \tag{B18}$$

On the other hand, calculating I_2:

$$I_2 = G_H V_2 - i_{2,\mathrm{out}} = G_H V_2 (1 - C_{RL}) - C_{RR} i_N \,, \tag{B19}$$

using now Eq. (B15c), this becomes a current division relation $I_2 = \mathcal{C}\, i_N$ where

$$\mathcal{C} = \frac{-C_{RR}C_{LL} - C_{LR} + C_{LR}C_{RL}}{C_{LL}} \,. \tag{B20}$$

Eqs. (B15a) to (B15b) then shows that $i_N = B_{RR} i_M$. We now use Eq. (B15a) to express i_M in terms of $G_H V_1$ and $G_H V_4$. Using Eq. (B18), we obtain :

$$i_N = \left(\frac{B_{RR} A_{RR}}{1 - B_{LR} A_{RL}} \right) G_H V_1 \,. \tag{B21}$$

This gives us the total current entering lead 2 in terms of the applied voltage V_1 at the right Ohmic contact:

$$I_2 = \mathcal{C} \frac{B_{RR} A_{RR}}{1 - B_{LR} A_{RL}} G_H V_1 \tag{B22}$$

Using one last time the voltage division relation (B18), the dimensionless impedance $z_{24} = Z_{24}^{(\mathrm{exp})}/R_H = G_H V_4/I_2$ is thus finally given by:

$$z_{24} = \frac{B_{LR}}{B_{RR} \times \mathcal{C}} \,. \tag{B23}$$

As in the three contact case, the fraction B_{LR}/B_{RR} appears in the results showing that the four point measurement does gives us information on the B quantum Hall bar. However, the matrix C is involved via the quantity $\mathcal{C}$. Nevertheless. it is possible to show that, to the lowest order frequency expansion, z_{24} does not depend on the physical relevant information contained within the C matrix. For this we once again use the low frequency expansion of the C scattering matrix (see Eq. (C12)):

$$C_{LL} = C_{RR} = 1 + C_{RL} \tag{B24}$$

$$C_{LR} = C_{RL} = \frac{-\mathrm{i}\omega l_C}{v_D(2 + \nu\alpha_\nu)} = -\mathrm{i}\omega\tau_C \tag{B25}$$

where l_C is the length of Hall bar C, and $\tau_C = \frac{l_C}{2v_D(1+\nu\alpha_\nu/2)}$ is the transit time across the Hall bar C. These formulas allow the calculation of quantity $\mathcal{C}$ from its definition by Eq. (B20) at the first order in $\omega\tau_C$:

$$\mathcal{C} = -1 + 2\mathrm{i}\omega\tau_C + o\left((\omega\tau_C)^2\right) \,. \tag{B26}$$

Finally, using Eq. (B23),

$$z_{24} = \frac{-\mathrm{i}\omega\tau_B}{(1 - i\omega\tau_B)(-1 + 2\mathrm{i}\omega\tau_C)} \simeq \mathrm{i}\omega\tau_B + o\left((\omega\tau_C)^2\right) \tag{B27}$$

showing that the measured inductance corresponds to the transit time in Hall bar B. Thus, the length involved in the determination of velocities is $l = l_B$.

Appendix C: Discrete element description from edge-magnetoplasmon scattering

In this Section, we present the computation of the EMP scattering matrix for an ungated quantum Hall bar and derive the corresponding description in terms of discrete elements valid at low frequency.

1. The model

We consider a quantum Hall bar of length l in the integer quantum Hall regime with filling fraction $\nu \geq 1$ as depicted on Fig. 8. We denote by R (resp. L) the upper (resp. lower) edge channels which are right (resp. left) movers as depicted on Fig. 8. We denote by $j_\alpha^{(\mathrm{in})}$ the incoming current entering the Hall bar on side $\alpha = R, L$ and $j_\alpha^{(\mathrm{out})}$ the outcoming one. Our goal is to relate the outcoming currents to the incoming ones in the presence of Coulomb interactions.

Here v_D denotes the bare drift velocity, which for simplicity we take identical for all edge channels. Coulomb interactions are described by assuming a discrete element model *à la* Christen-Büttiker [57] in which all the electrons within channels of the same chirality see the same time dependent potential $U_R(t)$ (for right movers) and $U_L(t)$ (for left movers). These potentials are related to

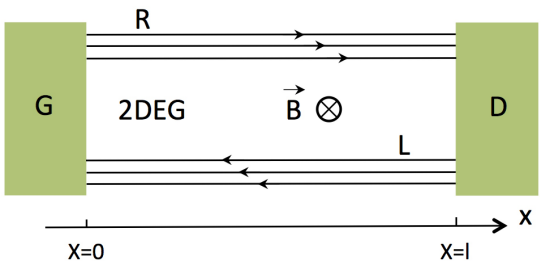

FIG. 8. A simple quantum Hall bar at filling fraction $\nu = 3$ connecting the G lead to the D lead. Along the R edge channels, electrons are right movers flowing from lead G to lead D whereas for edge channels L, they are left movers.

the total charge stored within the L and R edge channels by a capacitance matrix

$$\mathbf{Q} = \mathbf{C}\,\mathbf{U} \tag{C1}$$

in which

$$\mathbf{Q} = \begin{pmatrix} Q_R \\ Q_L \end{pmatrix}, \quad \mathbf{U} = \begin{pmatrix} U_R \\ U_L \end{pmatrix} \tag{C2}$$

and $\mathbf{C}$ denotes the capacitance matrix

$$\mathbf{C} = \begin{pmatrix} C_H & -\eta\, C_H \\ -\eta\, C_H & C_H \end{pmatrix}, \tag{C3}$$

where $0 \leq \eta \leq 1$ depending on the screening of Coulomb interaction between channels of opposite chiralities by nearby gates and other on-chip conductors. Eq. (C1) plays the role of a solution of the Poisson equation relating the electrical potential to the charge density. In this work, unless otherwise stated, we assume that the left and right chiral edge channels are in total influence and therefore that $\eta = 1$. The capacitance C_H can then be computed as the geometric capacitance of a stripline capacitor (see Sec. D).

The charges within the edge channels are directly related to the incoming and outcoming currents through charge conservation which, in the Fourier domain and in vector notation, is written as

$$\mathbf{j}^{(\mathrm{in})}(\omega) - \mathbf{j}^{(\mathrm{out})}(\omega) = -\mathrm{i}\omega\mathbf{Q}(\omega)\,. \tag{C4}$$

The last equation we need is the equation of motion for the charge or current density within the Hall bar [50]:

$$\mathbf{Q}(\omega) + C_q(l,\nu;\omega)\mathbf{U}(\omega) = \frac{l}{v_D}\, f\left(\frac{\omega l}{v_D}\right) \mathbf{j}^{(\mathrm{in})}(\omega)\,, \tag{C5}$$

in which $f(x) = (\mathrm{e}^{\mathrm{i}x} - 1)/\mathrm{i}x$, and

$$C_q(l,\nu;\omega) = \frac{\nu e^2 l}{h v_D}\, f\left(\frac{\omega l}{v_D}\right) \tag{C6}$$

represents the effective quantum capacitance at frequency $\omega/2\pi$ for the edge channels of length l and filling fraction ν. Eq. (C5) expresses that the charge stored within each edge channels comes from what is injected by the reservoirs and from the shift of the bottom of the electronic bands by the electric potential seen by all electrons.

2. Edge magnetoplasmon scattering

Using Eqs. (C1) and (C4) to eliminate $\mathbf{Q}(\omega)$ and $\mathbf{U}(\omega)$ from Eq. (C5) leads to

$$\begin{aligned}(C_q(l,\nu;\omega) + \mathbf{C})\,\mathbf{j}^{(\mathrm{out})}(\omega) = \\ \left(C_q(l,\nu;\omega) + \mathrm{e}^{\mathrm{i}\omega l/v_D}\mathbf{C}\right)\,\mathbf{j}^{(\mathrm{in})}(\omega)\,.\end{aligned} \tag{C7}$$

Solving this equation leads to the scattering matrix $S(\omega)$ relating incoming to outgoing electrical currents at ω. From the bosonization point of view, this is the scattering matrix for the bosonic counter-propagating edge-magnetoplasmon modes carrying the total charges of the ν right and ν left moving edge channels.

This scattering matrix depends on a dimensionless coupling constant α_ν characterizing the strength of Coulomb interactions within each edge channel by the way of the ratio of the bare quantum capacitance of a single edge channel with drift velocity v_D to the geometric capacitance [61]:

$$\alpha_\nu = \frac{C_q(l,\nu;\omega=0)}{C_H(l)\nu} = \frac{e^2 l/h v_D}{C_H(l)}\,. \tag{C8}$$

The higher this number, the higher is Coulomb's energy $e^2/C_H(l)$ with respect to the kinetic energy scale hv_D/l. The geometric capacitance can be evaluated using standard electrostatics as explained in Sec. D. The result comes under the form

$$C_H(l) = \varepsilon_0\varepsilon_r l\, f_{\mathrm{bar}}(W, W_H(\nu)) \tag{C9}$$

in which ε_r is the relative permittivity of the material and $f_{\mathrm{bar}}(W, W_H(\nu))$ is a geometrical factor that depends on the width W of the quantum Hall bar and on $W_H(\nu)$, the width of the system of ν copropagating edge channels at the edge of the quantum Hall bar. The latter is proportional to the filling fraction ν and, in the $W_H(\nu) \ll W$ limit, the geometric factor f_{bar} depends logarithmically on the aspect ratio $W/W_H(\nu)$ as shown in Sec. D. The dimensionless coupling constant

$$\alpha_\nu = \frac{2\,\alpha_{\mathrm{mat}}}{f_{\mathrm{bar}}(W, W_H(\nu))} \tag{C10}$$

is therefore proportional to the effective fine structure constant within the material

$$\alpha_{\mathrm{mat}} = \frac{e^2}{4\pi\varepsilon_r\varepsilon_0\hbar v_D} = \frac{\alpha_{\mathrm{qed}}}{\varepsilon_r}\,\frac{c}{v_D}\,. \tag{C11}$$

up to a subdominant logarithmic dependance in ν arising from classical electrostatics (see Sec. D). The ω dependence is an $X = \omega l/v_D$ dependence involving the free

electron time of flight l/v_D along the edges of the quantum Hall bar. Solving Eq. (C7) leads to the edge magnetoplasmon scattering amplitudes

$$S_{RL}(\omega) = S_{LR}(\omega) = \frac{-\mathrm{i}Xf(X)}{2+\nu\alpha_\nu f(X)} \tag{C12a}$$

$$S_{RR}(\omega) = S_{LL}(\omega) = 1 - S_{RL}(\omega)\,. \tag{C12b}$$

Note that the relation between diagonal and off diagonal S matrix elements given by Eq. (C12b) is only valid for total screening ($\eta = 1$). One should also note that because of the symmetric setup considered here, the edge magnetoplasmon scattering matrix is determined by its diagonal coefficient $S_\mathrm{d}(\omega) = S_{RR}(\omega) = S_{LL}(\omega)$ and its off-diagonal coefficient $S_\mathrm{od}(\omega) = S_{LR}(\omega) = S_{RL}(\omega)$. They satisfy the unitarity conditions

$$|S_\mathrm{d}(\omega)|^2 + |S_\mathrm{od}(\omega)|^2 = 1 \tag{C13a}$$

$$\mathrm{Re}(S_\mathrm{d}(\omega)S_\mathrm{od}(\omega)^*) = 0\,. \tag{C13b}$$

which ensure energy conservation within the quantum Hall bar.

3. Finite frequency impedances

In the spirit of Büttiker, let us derive a discrete element circuit description of the quantum Hall bar. In full generality, this description involves a three terminal circuit in order to take into account the electrostatic coupling to external gates which are assumed to be at the ground here (see Fig. 9). In our experimental, ungated samples, this coupling is expected to be small as we shall see. Note that the symmetry of the Hall bar under magnetic field reversal justifies considering two identical impedances $Z(\omega)$ on both sides of the central node A on Fig. 9. For this tri-terminal circuit, one can combine the relation between the potentials V_G, V_D, V_A and $V_0 = 0$ (by gauge invariance) and the current sum rule $I_G + I_D + I_0 = 0$ to relate I_G and I_D to V_G and V_D:

$$\begin{pmatrix} Z+Z_0 & Z_0 \\ Z_0 & Z+Z_0 \end{pmatrix} \cdot \begin{pmatrix} I_G \\ I_D \end{pmatrix} = \begin{pmatrix} V_G \\ V_D \end{pmatrix}. \tag{C14}$$

On the other hand, the finite frequency admittance of the quantum Hall bar can be obtained from the edge magnetoplasmon scattering matrix which, in the present case is symmetric. We can then infer expressions for the impedances $Z(\omega)$ and $Z_0(\omega)$ in terms of the EMP scattering matrix of the quantum Hall bar:

$$Z_0(\omega) = R_H\,\frac{S_\mathrm{d}(\omega)}{(1-S_\mathrm{od}(\omega))^2 - S_\mathrm{d}(\omega)^2}\,, \tag{C15a}$$

$$Z(\omega) = \frac{R_H}{1+S_\mathrm{d}(\omega)-S_\mathrm{od}(\omega)}\,. \tag{C15b}$$

Note that Eqs. (C15a) and (C15b) have been obtained without any explicit assumption of total screening. In the case of $\eta = 1$, Z_0 is expected to be infinite and is indeed found to be infinite since, in this case, $S_\mathrm{d}(\omega)+S_\mathrm{d}(\omega) = 1$ (see Eq. (C12b)).

To obtain the simplest effective circuit description, we just derive the dominant terms of the low frequency expansion of $Z(\omega)$ and $1/Z_0(\omega)$ by expanding the edge-magnetoplasmon scattering matrix in powers of ω. This leads to $1/Z_0(\omega) = 0$ (total screening) and

$$Z(\omega) = \frac{R_H}{2}\left(1 - \frac{\mathrm{i}\omega l/v_D}{2+\nu\alpha_\nu}\right) \tag{C16}$$

which shows that the impedance $Z(\omega)$ can be viewed as the series addition of a resistance $R_H/2$ (ν parallel single channel contact resistances $R_K/2$) and an inductance L_Z such that

$$\frac{2L_Z}{R_H} = \frac{l/2\,v_D}{1+\nu\alpha_\nu/2}\,. \tag{C17}$$

The quantum Hall bar is then a dipole with impedance $2Z(\omega)$ which then behaves as an inductance in series with the quantum Hall resistance R_H at low frequency. Since $2L_Z$ is the total inductance L of the quantum Hall bar, it follows that the electronic time of flight l/v_D appearing in Eq. (A4) is renormalized by Coulomb interactions. The corresponding renormalized velocity

$$v_0 = v_D\,\left(1+\frac{\nu\alpha_\nu}{2}\right) \tag{C18}$$

can, in a sense, be interpreted as an effective charge velocity.

To understand this more precisely, let us imagine that the quantum Hall bar could be viewed as an ideal coaxial cable with ν channels with plasmonic velocity v_P. This would lead to a diagonal plasmon scattering matrix: $S_\mathrm{od}(\omega) = 0$ and $S_\mathrm{d}(\omega) = \mathrm{e}^{\mathrm{i}\omega l/v_P}$. The corresponding admittance $Z(\omega)$ would then be given by

$$Z_\mathrm{tl}(\omega) = \frac{R_H}{2}\,\frac{1}{1+\mathrm{e}^{\mathrm{i}\omega l/v_P}} \tag{C19}$$

where the index tl emphasizes the transmission line description considered here. Its low frequency expansion would correspond to the series addition of the contact resistance $R_H/2$ with an inductance $L_Z^{(\mathrm{tl})}$ given by

$$\frac{2L_Z^{(\mathrm{tl})}}{R_H} = \frac{l}{2\,v_P}\,. \tag{C20}$$

Consequently, we also recover the analogue of Eq. (A4) with v_P playing the role of v_D. However, in this transmission line model, the admittance $1/Z_0$ would not vanish, thereby showing that such a transmission line model cannot describe the totally screened situation. The edge magnetoplasmon scattering matrix derived in Sec. C 2 shows that, in the totally screened case, R_H/Z_0 vanishes.

Appendix D: Geometric capacitance

In this section, we compute the geometric capacitance of the quantum Hall bar using a model a capacitor

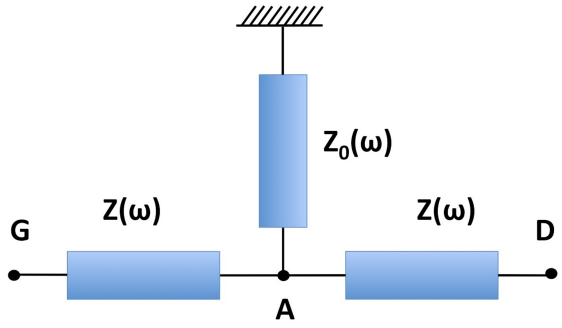

FIG. 9. The lumped element circuit equivalent to simple quantum Hall bar depicted on Fig. 8. The 0 lead corresponds to metallic gates and conductors to which the edge channels are capacitively coupled in the case of partial mutual capacitive coupling between the R and L channels ($\eta < 1$). We expect $\mathrm{Re}(Z(\omega)) = R_H/2$ and $\mathrm{Im}(Z(\omega))$ to be inductive at low frequency whereas $\mathrm{Re}(Z_0(\omega)) = 0$ and $Z_0(\omega)$ is expected to be capacitive in general, and to be infinite in the totally screened case ($\eta = 1$).

built from two coplanar strips corresponding to the two counter-propagating edge channel systems.

1. Width of edge channels

The model of Ref. [27] by Schklovskii *et al.* describes the structure of quantum Hall edge channels when taking into account the effect of Coulomb interactions. It predicts the width λ_H (denoted by a_ν in Ref. [27]) of the incompressible channels in term of the density gradient at the edge as well as the width b_ν of compressible channels as a function of λ_H.

The width of incompressible stripes is obtained by identifying the Landau gap with the energy variation of an electron in the confining potential U (see Figure 10):

$$a_\nu \times e\nabla U = \hbar\frac{eB}{m^*} \quad , \tag{D1}$$

where ∇U denotes the gradient of U at the edge of the sample. This leads to:

$$a_\nu = \frac{\hbar}{m^* v_D} \, , \tag{D2}$$

where we have defined $v_D = E_y/B_z$ as the drift velocity along the edge. Note that this expression is formally the Compton wavelength associated with a relativistic particle of mass m^* and effective speed of light v_D. This explains why we denote it by λ_H in the following. This result is not surprising, the width of the incompressible stripe is the minimal one for closing the cyclotron gap for an electronic excitation in the confinement potential, as shown in Ref. [27].

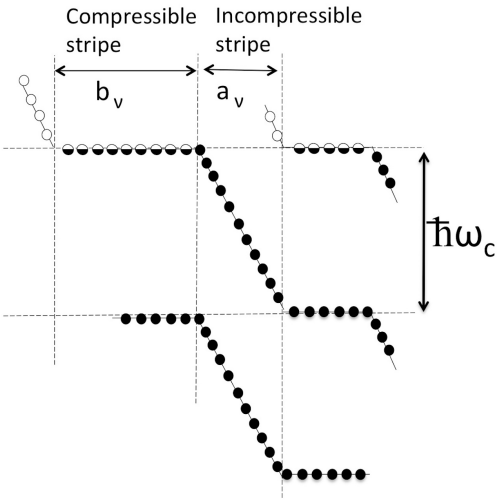

FIG. 10. Edge channel structure arising from Coulomb interaction effects in a mean field theory approach [27]: incompressible stripes alternate with compressible stripes in which electrons are located right at the Fermi energy.

Once the width of an incompressible stripe is known, the width of a compressible stripe is

$$b_\nu = \frac{\pi}{4}\frac{\lambda_H^2}{a_B} \tag{D3}$$

where $a_B = \hbar^2\varepsilon/m^*e^2$ denotes the effective Bohr radius in the material.

2. Capacitance computation

The quantum Hall edge channel system has a width

$$W_H(\nu) = \frac{\nu\hbar}{m^* v_D}\left(1 + \pi^2\alpha_{\mathrm{mat}}\right) \, , \tag{D4}$$

which is of the order of 90 nm per edge channel in AlGaAs/GaAs systems. In the transverse direction, the electrons are confined within a triangular potential well. The typical extension of the electron's wavefunction in the transverse direction is of the order of 5 nm [62], therefore suggesting a rather flat shape of the edge channel.

A first estimate of the geometric capacitance of the edge channel system can thus be obtained by computing the geometric capacitance per unit of length of an infinite pair of coplanar strips of width w separated by a distance d [63]:

$$\frac{C_H(l)}{l} = \varepsilon_0\varepsilon_r \frac{\mathrm{K}(\sqrt{1-x^2})}{\mathrm{K}(x)} \, , \tag{D5}$$

in which $\mathrm{K}(x)$ denotes the elliptic integral of the first kind [64] evaluated at $x = d/(d+2w)$ where, in our

case $w = W_H(\nu)$ and $d + 2w = W$ is the total width of the quantum Hall bar. Using known asymptotics for the elliptic integral, we find the geometrical capacitance for the quantum Hall bar of width W and length l at filling fraction ν

$$C_H(\nu, l) \simeq \frac{\pi\varepsilon_0\varepsilon_r l}{\ln\left[\frac{W}{8W_H(\nu)}\right]}\,. \tag{D6}$$

On the other hand, using a more precise self-consistant solution of the electrical potential within quantum Hall edge channel arising from the repartition of quantum electrons, Hirai and Komiyama [51] have shown that the capacitance can be obtained as the geometric capacitance of two parallel wires:

$$c_0'(\nu, l) = \frac{\pi\varepsilon_0\varepsilon_r l}{\ln\left(\frac{\mathrm{e}\,W}{2W_H(\nu)}\right)}\,. \tag{D7}$$

Expressions (D6) and (D7) are not identical, but both are considered in the regime where $W \gg W_H(\nu)$, that is, when they lead to similar estimates for the capacitance. Both expressions are of the form

$$C_H(\nu, l, \gamma) = \frac{\pi\varepsilon_0\varepsilon_r l}{\ln\left(\frac{\gamma W}{W_H(\nu)}\right)}\,, \tag{D8}$$

where γ is a factor that depends on the specific model used to describe the charge repartition within the edge channels. Here $\gamma = \mathrm{e}/2$ in Harai *et al.*'s estimate and $\gamma = 1/8$ for the coplanar strip capacitance model. Using Eq. (D8), the effective coupling constant is then

$$\alpha_\nu = \frac{2\alpha_{\rm mat}}{\pi}\left[\ln\left(\frac{\gamma\, W/\lambda_H}{(1+\pi^2\alpha_{\rm mat})\nu}\right)\right]. \tag{D9}$$

Using this expression into Eq. (C18) leads to

$$\frac{v_0}{v_D} = 1 + \frac{\nu\alpha_{\rm mat}}{\pi}\ln\left(\frac{\gamma W/\lambda_H}{(1+\pi^2\alpha_{\rm mat})\nu}\right) \tag{D10}$$

for the ratio of v_0 to the drift velocity within a chiral edge channel. This expression can then be rewritten in terms of the effective single edge channel width $\xi_H = (1+\pi^2\alpha_{\rm mat})\lambda_H/\gamma$:

$$\frac{v_0}{v_D} = 1 + \frac{\nu\alpha_{\rm mat}}{\pi}\ln\left(\frac{W/\xi_H}{\nu}\right) \tag{D11}$$

Appendix E: Supplementary results

In this Section, we show further experimental results obtained on sample A (the sample discussed in the paper) and on three other samples manufactured from three different AlGaAs/GaAs heterojunctions. Their wafer characteristics (electron density and mobility of the two-dimensional electron gas) are reported in table I. Samples have been processed on these heterojunctions using the same design and dimensions as for sample A. Exeperimental results obtained on these samples have been obtained using exactly the same protocols and they are completely similar to the results presented in the paper.

We first present complementary results on sample A, then we present results obtained on the other samples, which concern influence of filling factor ν and influence of edge channel length.

Wafer	$N_s(\mathrm{cm}^{-2})$	$\mu(\mathrm{m}^2/\mathrm{Vs})$	B (for $\nu = 2$)	Width (µm)
A	5.1	30	10.5 T	400
B	3.3	50	6.8 T	1600
C	4.5	55	9.2 T	400
D	4.3	42	9 T	800

TABLE I. Sample characteristics: carrier density, mobility, magnetic field at $\nu = 2$ and width of Hall bars.

1. Complementary results on sample A

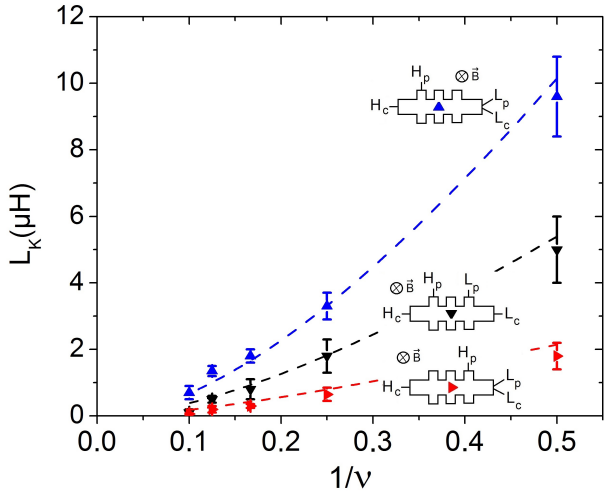

FIG. 11. Kinetic Inductance as a function of the inverse of filling factor for a negative orientation of magnetic field . Dashed line represents the theoretical model (Eq.(1) of the paper) with following parameters : $v_D = 8\times10^5\,\mathrm{ms}^{-1}$ for the larger configuration, $v_D = 11\times10^5\,\mathrm{ms}^{-1}$ for the intermediate one, $v_D = 22\times10^5\,\mathrm{ms}^{-1}$ for the short one. Length of edge states are still the same (see Fig. 3 of the paper).

Fig. 3 of the paper shows, for a positive orientation of magnetic field, the dependence of the quantum inertia on the inverse of the filling factor. In Fig. 11 of this Supplementary Material, these results have been obtained for a negative orientation of magnetic field. Dashed curves are obtained using Eq. (1) of the paper, using a proper velocity v_D for each configuration (see caption).

2. Influence of filling factor for other samples

For sample A we have shown that reactance increases linearly with frequency and that the slope depends strongly on the filling factor. Here, we observe the same behavior on other samples (see Figs. 12 to 15): the slope decreases while the filling factor increases.

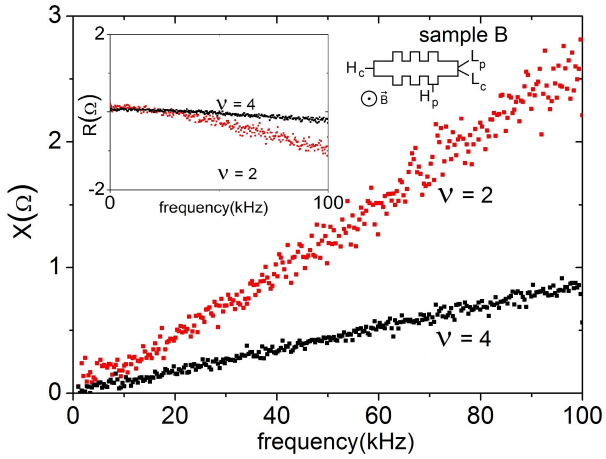

FIG. 12. Reactance as a function of frequency, for sample B and $\nu = 4$ and 4. Configuration is shown in inset.

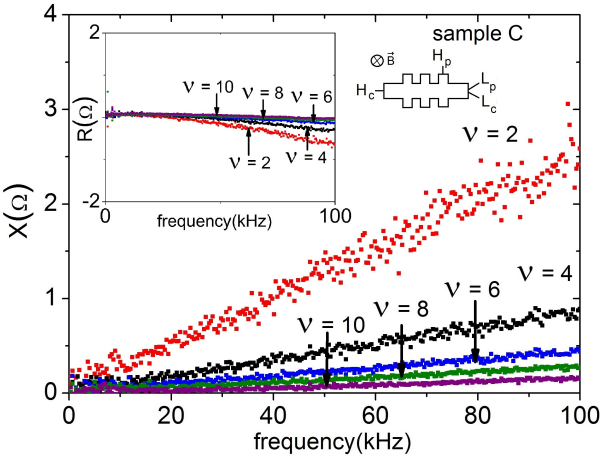

FIG. 13. Reactance as a function of frequency, for sample C and $\nu = 2$ to 10 by steps of 2. Configuration is shown in inset.

For all samples and configurations the inductance decreases with density of states. Quantum inertia appears then to be a robust effect against variability of experimental conditions, even in macroscopic samples. Still, the dependence of the inductance on the filling factor is not fully linear. These results corroborates the conclusions obtained from sample A : the velocity v_0 depends on the filling factor.

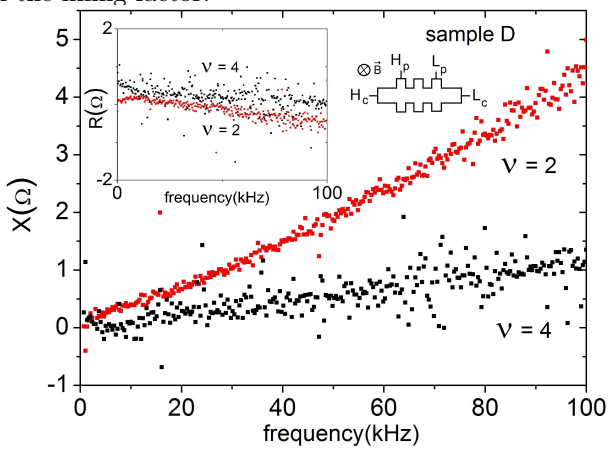

FIG. 14. Reactance as a function of frequency, for sample D and $\nu = 2$ and 4. Configuration is shown in inset.

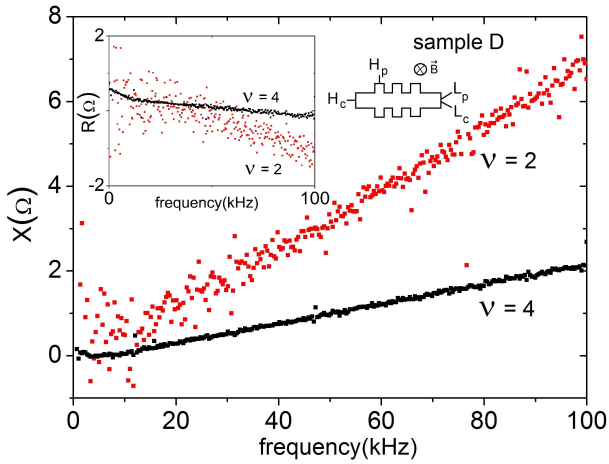

FIG. 15. Reactance as a function of frequency, for sample D at $\nu = 2$ and 4 and configuration shown in inset.

3. Influence of configurations for other samples

Figs. 16 to 19 depict the reactance as a function of frequency for three samples at different filling factors. For each sample at a given filling factor, we observe how the configuration (shown as an inset for each curve) modifies the slope of the reactance. Each configuration has its proper length and the larger the edge states the higher the quantum inertia. The length concerned here is the distance between potentials L_p and H_p.

Meanwhile, differences in velocity v_D for distinct configurations imply that the ratio between quantum inertia and length of edge states not a constant. Configurations are obtained after wire-bonding the samples. This entails heating the samples and cool them down again afterwards, and this causes the velocity v_0 to change a bit from one configuration to another.

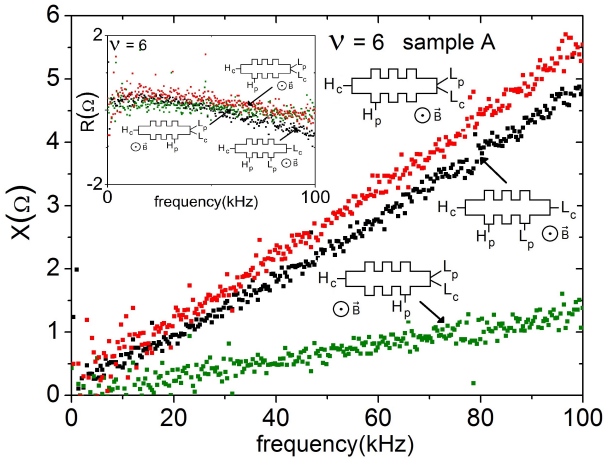

FIG. 16. Reactance as a function of frequency, for sample A at $\nu = 6$ and for the three configurations.

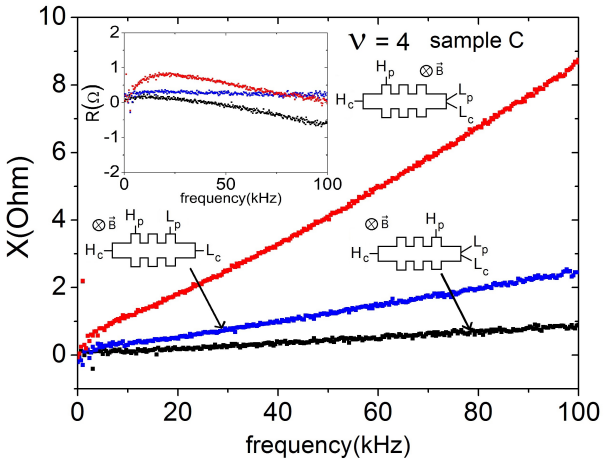

FIG. 17. Reactance as a function of frequency, for sample C at $\nu = 4$ and for the three configurations.

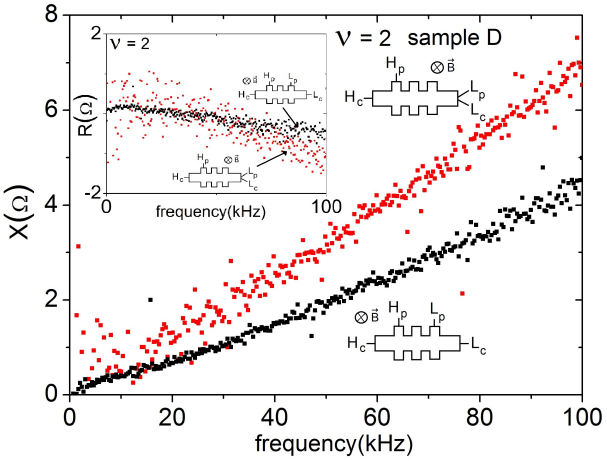

FIG. 18. Reactance as a function of frequency for sample D at $\nu = 2$ for two configurations.

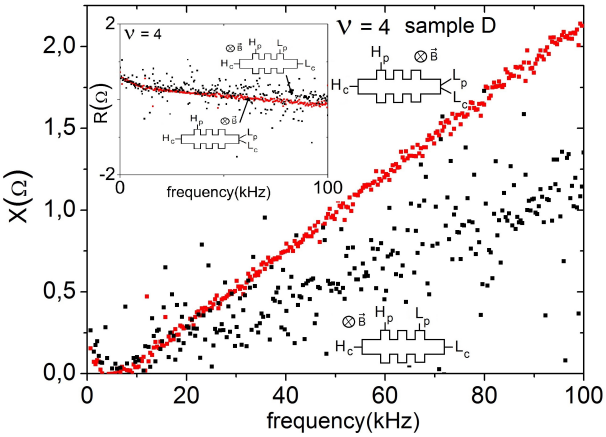

FIG. 19. Reactance as a function of frequency for sample D at $\nu = 4$ for two configurations. Note the smaller values for $X(\Omega)$ compared to the other curves which may explain the more noisy dataset for the four-terminal geometry.

[1] K. v. Klitzing, G. Dorda, and M. Pepper, Phys. Rev. Lett. **45**, 494 (1980).
[2] B. Halperin, Phys. Rev. B **25**, 2185 (1982).
[3] R. J. Haug, Semiconductor Science and Technology **8**, 131 (1993).
[4] J. Weis and K. von Klitzing, Philosophical Transactions of the Royal Society A: Mathematical, Physical and Engineering Sciences **369**, 3954 (2011).
[5] M. E. Suddards, A. Baumgartner, M. Henini, and C. J. Mellor, New Journal of Physics **14**, 083015 (2012).
[6] C. I. des Poids et Mesures, "Représentation de l'ohm à partir de l'effet hall quantique," Recom. 2 (CI-1988) 77th Session (1988).
[7] B. Jeckelmann and B. Jeanneret, Reports on Progress in Physics **64**, 1603 (2001).
[8] F. J. Ahlers, B. Jeanneret, F. Overney, J. Schurr, and B. M. Wood, Metrologia **46**, R1 (2009).
[9] F. Delahaye, Metrologia **31**, 367 (1995).
[10] S. W. Chua, A. Hartland, and B. Kibble, IEEE Transactions on Instrumentation and Measurement **48**, 309 (1999).
[11] J. Schurr, B. Wood, and F. Overney, IEEE Transactions on Instrumentation and Measurement **54**, 512 (2005).
[12] M. E. Cage and A. Jeffrey, J. Res. Natl. Inst. Stand. Technol. **101**, 733 (1996).
[13] B. Jeanneret, B. D. Hall, H.-J. Bühlmann, R. Houdré, M. Ilegems, B. Jeckelmann, and U. Feller, Phys. Rev. B **51**, 9752 (1995).
[14] J. Schurr, J. Kučera, K. Pierz, and B. P. Kibble, Metrologia **48**, 47 (2011).
[15] P. J. Burke, IEEE Transactions on Nanotechnology **1**, 129 (2002).
[16] J. Kang, Y. Matsumoto, X. Li, J. Jiang, X. Xie, K. Kawamoto, M. Kenmoku, J. H. Chu, W. Liu, J. Mao, K. Ueno, and K. Banerjee, Nature Electronics **1**, 46 (2018).
[17] A. A. Annunziata, D. F. Santavicca, F. Frunzio, G. Catelani, M. J. Rooks, A. Frydman, and D. E. Prober, Nanotechnology **21**, 445202 (2010).
[18] J. Luomahaara, V. Vesterinen, L. Grönberg, and J. Hassel, Nature Communications **5**, 4872 (2014).
[19] G. Coiffard, K. F. Schuster, E. F. C. Driessen, S. Pignard, M. Calvo, A. Catalano, J. Goupy, and A. Monfardini, Journal of Low Temperature Physics **184**, 654 (2016).
[20] M. Büttiker, A. Prêtre, and H. Thomas, Phys. Rev. Lett. **70**, 4114 (1993).
[21] M. Büttiker, J. Phys.: Condens. Matter **5**, 9361 (1993).
[22] A. Prêtre, H. Thomas, and M. Büttiker, Phys. Rev. B **54**, 8130 (1996).
[23] J. Gabelli, G. Fève, J. Berroir, B. Plaçais, A. Cavanna, B. Etienne, Y. Jin, and D. Glattli, Science **313**, 499 (2006).
[24] J. Gabelli, G. Fève, T. Kontos, J.-M. Berroir, B. Plaçais, D. Glattli, B. Etienne, Y. Jin, and M. Büttiker, Phys. Rev. Lett. **98**, 166806 (2007).
[25] L. Song, J. Yin, and S. Chen, New Journal of Physics **20**, 053059 (2018).
[26] S. M. Girvin and K. Yang, *Modern Condensed Matter Physics* (Cambridge university Press, 2019).
[27] D. Chklovskii, B. Shklovskii, and L. Glazman, Phys. Rev. B **46**, 4026 (1992).
[28] M. Hashisaka, H. Kamata, N. Kumada, K. Washio, R. Murata, K. Muraki, and T. Fujisawa, Phys. Rev. B **88**, 235409 (2013).
[29] N. Hiyama, M. Hashisaka, and T. Fujisawa, Applied Physics Letters **107**, 143101 (2015).
[30] B. Kibble and G. Rayner, *Coaxial AC bridges* (Taylor & Francis, 1984).
[31] *Agilent impedance measurement handbook* (Agilent Technologies Inc., 2009).
[32] M. Grayson and F. Fischer, Journal of Applied Physics **98**, 013709 (2005).
[33] C. Hernandez, C. Consejo, P. Degiovanni, and C. Chaubet, Journal of Applied Physics **115**, 123710 (2014).
[34] W. Desrat, D. K. Maude, L. B. Rigal, M. Potemski,

J. C. Portal, L. Eaves, M. Henini, Z. R. Wasilewski, A. Toropov, G. Hill, and M. A. Pate, Phys. Rev. B **62**, 12990 (2000).
[35] J. Melcher, J. Schurr, F. m. c. Delahaye, and A. Hartland, Phys. Rev. B **64**, 127301 (2001).
[36] Here $R_{xx}(\omega)$ denotes the frequency dependant longitudinal dependence of the quantum Hall bar.
[37] I. Safi and H. Schulz, Phys. Rev. B **52**, R1740 (1995).
[38] I. Safi, Eur. Phys. J. **D 12**, 451 (1999).
[39] I. Safi and H. Schulz, in *Quantum Transport in Semiconductor Submicron Structures*, edited by B. Kramer (Kluwer Academic Press, Dordrecht, 1995) p. 159.
[40] H. Steinberg, G. Barak, A. Yacobi, L. Pfeiffer, K. West, B. Halperin, and K. Le Hur, Nature Physics **4**, 116 (2008).
[41] H. Kamata, N. Kumada, M. Hashisaka, K. Muraki, and T. Fujisawa, Nature Nanotechnology **9**, 177 (2014).
[42] P. Brasseur, N. H. Tu, Y. Sekine, K. Muraki, M. Hashisaka, T. Fujisawa, and N. Kumada, Phys. Rev. B **96**, 081101 (2017).
[43] G. Roussely, E. Arrighi, G. Georgiou, S. Takada, M. Schalk, M. Urdampilleta, A. Ludwig, A. D. Wieck, P. Armagnat, T. Kloss, X. Waintal, T. Meunier, and C. Bäuerle, Nature Communications **9**, 2811 (2018).
[44] D. C. Glattli, E. Y. Andrei, G. Deville, J. Poitrenaud, and F. I. B. Williams, Phys. Rev. Lett. **54**, 1710 (1985).
[45] G. Sukhodub, F. Hohls, and R. J. Haug, Phys. Rev. Lett. **93**, 196801 (2004).
[46] S. Mikhaelov, "Edge excitations of low dimensional charged systems," (Nova science Publishers Inc., Hutungton, New York, 2000) Chap. 1, pp. 1 – 49.
[47] M. Hashisaka, K. Washio, H. Kamata, K. Muraki, and T. Fujisawa, Phys. Rev. B **85**, 155424 (2012).
[48] P. Degiovanni, C. Grenier, G. Fève, C. Altimiras, H. le Sueur, and F. Pierre, Phys. Rev. B **81**, 121302(R) (2010).
[49] R. Rodriguez, F. Parmentier, D. Ferraro, P. Roulleau, U. Gensser, A. Cavanna, M. Sassetti, F. Portier, D. Mailly, and P. Roche, Nature Communications **11**, 2426 (2020).
[50] C. Cabart, B. Roussel, G. Fève, and P. Degiovanni, Phys. Rev. B **98**, 155302 (2018).
[51] H. Hirai and S. Komiyama, Phys. Rev. B **49**, 14012 (1994).
[52] N. Kumada, H. Kamata, and T. Fujisawa, Phys. Rev. B **84**, 045314 (2011).
[53] D. T. McClure, Y. Zhang, B. Rosenow, E. M. Levenson-Falk, C. M. Marcus, L. N. Pfeiffer, and K. W. West, Phys. Rev. Lett. **103**, 206806 (2009).
[54] E. Bocquillon, V. Freulon, F. Parmentier, J. Berroir, B. Plaçais, C. Wahl, J. Rech, T. Jonckheere, T. Martin, C. Grenier, D. Ferraro, P. Degiovanni, and G. Fève, Ann. Phys. (Berlin) **526**, 1 (2014).
[55] A. L. Grimsmo, F. Qassemi, , B. Reulet, and A. Blais, Phys. Rev. Lett. **116**, 043602 (2016).
[56] E. B. Rosa, Bulletin of the Bureau of Standards **4**, 301 (1908).
[57] T. Christen and M. Büttiker, Phys. Rev. B **53**, 2064 (1996).
[58] D. Ferraro, B. Roussel, C. Cabart, E. Thibierge, G. Fève, C. Grenier, and P. Degiovanni, Phys. Rev. Lett. **113**, 166403 (2014).
[59] A. Delgard, B. Chenaud, D. Mailly, U. Gennser, K. Ikushima, and C. Chaubet, Physica Status Solidi B **256**, 1800548 (2019).
[60] A. O. Slobodeniuk, I. P. Levkivskyi, and E. V. Sukhorukov, Phys. Rev. B **88**, 165307 (2013).
[61] The l dependance of C_H is restored here to stress that we are in the limit of a long quantum Hall bar ($l \gg W$) where it is linear in l.
[62] F. F. Fang and W. E. Howard, Phys. Rev. Lett. , 797 (1966).
[63] Y. Y. Iossel, E. Kochanov, and M. G. Strunsjkiy, *The calculation of electrical capacitance*, Tech. Rep. (Leningradskoye Otdeleniye "Energiya"., 1969).
[64] I. Gradshteyn and I. Ryzhik, *Table of integrals, series and products (fifth ed.)* (Academic Press, Inc, 1994).